Article

DFT Simulation-Based Design of 1T-MoS$_2$ Cathode Hosts for Li-S Batteries and Experimental Evaluation

Elaheh Hojaji [1,2], Eleftherios I. Andritsos [1,2], Zhuangnan Li [3], Manish Chhowalla [3], Constantina Lekakou [1,*] and Qiong Cai [2,*]

[1] Department of Mechanical Engineering Sciences, Faculty of Engineering and Physical Sciences, University of Surrey, Guildford GU2 7XH, UK
[2] Department of Chemical and Process Engineering, Faculty of Engineering and Physical Sciences, University of Surrey, Guildford GU2 7XH, UK
[3] Department of Materials Science and Metallurgy, University of Cambridge, Cambridge CB3 0FS, UK
[*] Correspondence: c.lekakou@surrey.ac.uk (C.L.); q.cai@surrey.ac.uk (Q.C.)

Abstract: The main challenge in lithium sulphur (Li-S) batteries is the shuttling of lithium polysulphides (LiPSs) caused by the rapid LiPSs migration to the anode and the slow reaction kinetics in the chain of LiPSs conversion. In this study, we explore 1T-MoS$_2$ as a cathode host for Li-S batteries by examining the affinity of 1T-MoS$_2$ substrates (pristine 1T-MoS$_2$, defected 1T-MoS$_2$ with one and two S vacancies) toward LiPSs and their electrocatalytic effects. Density functional theory (DFT) simulations are used to determine the adsorption energy of LiPSs to these substrates, the Gibbs free energy profiles for the reaction chain, and the preferred pathways and activation energies for the slow reaction stage from Li$_2$S$_4$ to Li$_2$S. The obtained information highlights the potential benefit of a combination of 1T-MoS$_2$ regions, without or with one and two sulphur vacancies, for an improved Li-S battery performance. The recommendation is implemented in a Li-S battery with areas of pristine 1T-MoS$_2$ and some proportion of one and two S vacancies, exhibiting a capacity of 1190 mAh/g at 0.1C, with 97% capacity retention after 60 cycles in a schedule of different C-rates from 0.1C to 2C and back to 0.1C.

Keywords: Li-S battery; cathode; 1T-MoS$_2$; sulphur vacancy; reaction pathway

1. Introduction

The rechargeable lithium-sulphur (Li-S) batteries feature the advantages of high theoretical energy density, low toxicity, and low cost, making them promising candidates as the next-generation energy storage technology. Despite extensive development in materials for the cathode, separator, and electrolyte [1], the migration of lithium polysulphides (LiPSs) to the anode and the slow reaction kinetics are still the key challenges that hinder their commercial applications. The impact of the LiPSs migration and shuttling effect is active material loss, rapid capacity fading, poor cycling stability, and severe anode corrosion [2]. Although a solid electrolyte would not allow any shuttling of LiPSs [3], it would also substantially reduce the diffusion rate of the Li$^+$ ions [3–5], compared to that of cations in liquid electrolytes [5,6]. Efforts to eliminate the problem of LiPSs migration while using a liquid electrolyte have focussed on trapping the soluble LiPSs in the cathode via physical confinement or attraction to functional groups in the cathode host. Nanostructured cathode hosts of hollow carbon particles [7] and micro/mesoporous carbon [8,9] offer physical confinement, despite their limited sulphur loading and inability of cyclic S$_8$ to fill ultra-micropores [10,11], where the redox reactions and Li$^+$ ion diffusion are expected to take place on the solid surface [12]. Added functional groups such as -OH, -COOH, and -NH$_2$ or N- and O- doped carbon have also shown an increased adsorption energy for the carbonaceous hosts in relation to LiPSs, with the adsorption energy predicted to be in the range of 0.5 to 2 eV via density functional theory (DFT) simulations [13–15].

Cathode hosts that both trap LiPSs and also act as electrocatalysts are of the greatest interest for the Li-S batteries: trapping LiPSs slows down their migration, while a fast redox reaction to the next stage in the reaction chain ensures a longer discharge curve to higher capacity. Single atom catalysts (SACs) of TM–N_4–C (TM = Co, Fe, V, and W) are of this type, showing promise of good electrocatalysts with the DFT-predicted adsorption energies of soluble LiPSs in the range of 1.3 to 4.3 eV [16–19]. However, a low concentration (1–2 at.%) of these single atoms can be achieved in practice in real materials without particle segregation, which makes it challenging if high loading of single atoms for high overall performance is aimed [20]. Polar hosts, such as transition-metal carbides [21,22], oxides/hydroxides [23,24], sulphides [25,26], selenides [27], nitrides, phosphides [28], and their composites [29,30] instead prove to be more promising to enhance the anchoring capability towards polysulphides intermediates and the kinetics of the LiPSs redox reactions, as they act across the full material surface. Among the polar materials, however, only metal sulphides exhibit enhanced electronic conductivity and catalytic properties at a very high kinetic rate of sulphur electrochemistry during cell operation [31–33].

The 2D dichalcogenide MoS_2, as one of the polar metal sulphide hosts with high electrochemical activity, has recently gained attention to direct the polysulphide conversion reaction to an energetically favourable pathway, leading to significantly enhanced redox kinetics and improved cyclic stability [34–36]. Different polytype phase transitions for MoS_2 have been reported, including 2H (hexagonal) and 1T (triangular) MoS_2 [37–39], of which 1T-MoS_2 has superior electronic conductivity. From the former category, several hybrid constructions have been suggested such as 2H-MoS_2/rGO [40], 2H-MoS_2-graphene nanocomposites [41], sulphur/copolymer/2H-MoS_2 [42], 2H-MoS2@HCS [43], and 2H-MoS_2/S prepared by decomposing $(NH_4)_2MoS_4$ [44]. The remarkable catalytic properties of 1T-MoS_2 and strong anchoring sites for LiPSs encouraged its employment in the form of nanodots in Li-S batteries, which yielded 721 mAh g_S^{-1} after 300 cycles, while a low electrolyte/sulphur ratio of 4.6 μL mg^{-1} was used [45]. The reported hybrid constructions on 1T-MoS_2 have been MXene/1T-MoS_2 nanohybrids [46], SnO_2/1T-MoS_2 nanoarray [35] and three-dimensional graphene/1T-MoS_2 (3DG/TM) heterostructure [47]. The sulphur deficiency in the structure of 2H-MoS_2 has also been suggested to significantly enhance polysulphides conversion compared with the plain MoS_2, as a result of providing more kinetically driving force and formation of more thermodynamically stable structures, such as hybrid constructions of reduced graphene oxide (2H-MoS_2–x/rGO) [48] and hollow mesoporous carbon (2H-MoS_2-x/HMC) [32]. Nevertheless, no study has been conducted so far on the role of defected structures of 1T-MoS_2 as the cathode host compared with the pristine 1T-MoS_2, necessitating a profound theoretical understanding of the anchoring effects toward LiPSs components and the catalytic effects for the redox reactions.

The literature provides a number of DFT simulations on different MoS_2-based hosts to boost the anchoring effect of the pristine 2H-MoS_2 toward LiPSs and therefore reduce its dissolution in the chosen electrolyte [26,47,49–51]. The DFT predicted adsorption energies of LiPSs by a pristine 1T-MoS_2 monolayer were also reported in the range of 0.64 to 2.9 eV, compared with 0.1 to 0.8 eV by a pristine 2H-MoS_2 monolayer [26]. In a separate study, the calculated adsorption energies of LiPSs adsorbed on a pristine 1T-MoS_2 monolayer were reported in the range of 1.1 to 1.4 eV, which were significantly higher than those of graphene supported 1T-MoS_2 and free-standing graphene [47]. Despite different reported values of adsorption energies for pristine 1T-MoS_2, research is still ongoing for an ideal anchoring material with enhanced electrocatalytic effects, good electrical and ionic conductivity, improving the electrochemical performance of Li–S batteries. To our knowledge, the binding effects of the defected 1T-MoS_2 structures towards LiPSs have not yet been explored. Additionally, the catalytic activity for the LiPSs conversion reactions on the sulphur-deficient 1T-MoS_2 structures is not known, although the conversion reaction of LiPSs on 2H-MoS_2 and 2H-MoS_2-2S during the discharge process [51], has been studied using the Gibbs free energy profiles.

In this study, we use DFT simulations to design 1T-MoS$_2$ hosts for Li-S batteries by assessing a pristine 1T-MoS$_2$ substrate, an 1T-MoS$_2$-1S (with one sulphur vacancy) and an 1T-MoS$_2$-2S (with two sulphur vacancies) in terms of their binding energy with LiPSs, the Gibbs free energy profiles for the full polysulphide reaction chain from S$_8$ to Li$_2$S to identify the rate-limiting step in the conversion reactions, and the reaction pathway from Li$_2$S$_4$ to Li$_2$S, as this section of the pathway is considered the flattest part of the profile with rate-limiting sections [17]. The TSS (transition state search) task of DFT is employed to predict the activation energy barriers to chemical reactions to determine reaction pathways for the typically slow reaction chain of Li$_2$S$_4$ to Li$_2$S$_2$ and then to Li$_2$S for the different 1T-MoS$_2$ substrates. Furthermore, a Li-S battery is evaluated experimentally with a 1T-MoS$_2$ cathode host combining the structures investigated in DFT, then its performance is compared to a typical sulphur cathode with a carbonaceous host.

2. Results and Discussion

2.1. DFT Simulations

The optimised 1T-MoS$_2$ and its defected (MoS$_2$-1S and MoS$_2$-2S) structures, as well as the optimised configurations of Li$_2$S$_n$ (n = 1, 2, 4, 6, and 8), are shown in Figure 1. All structures and the average bond lengths are in a good agreement with high-accuracy first-principles calculations reported so far [17,52].
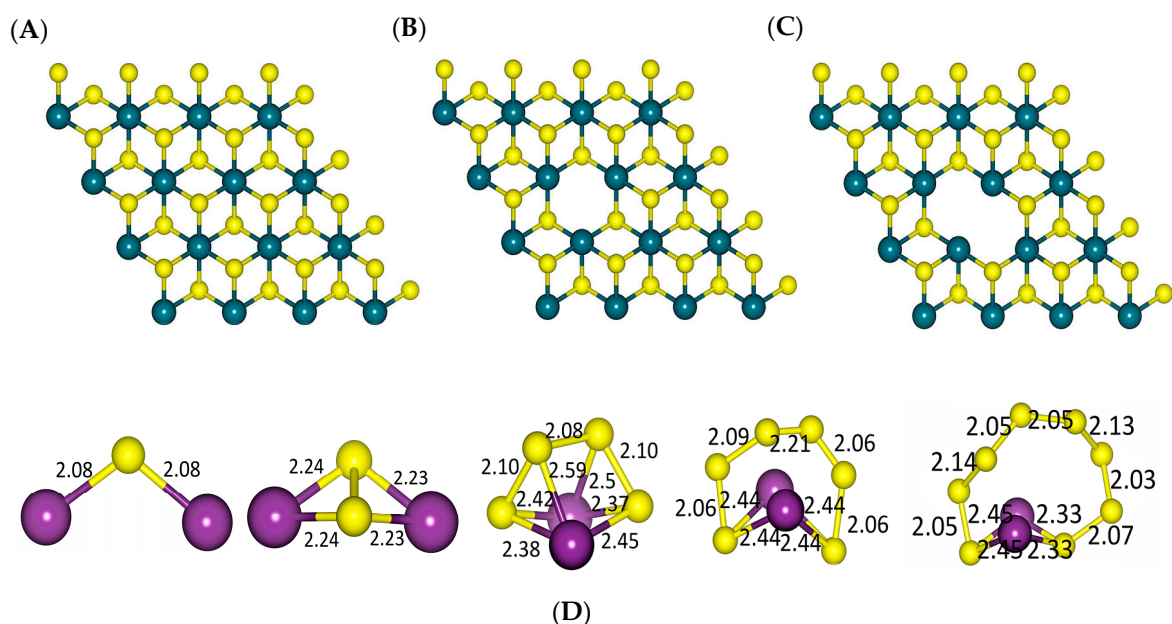

Figure 1. The optimized structures of (**A**) 1T-MoS$_2$, (**B**) 1T-MoS$_2$-1S, and (**C**) 1T-MoS$_2$-2S and (**D**) Li$_2$S$_n$ (n = 1, 2, 4, 6, and 8), where teal, violet, and yellow colours denote Mo, Li, and S atoms, respectively. Atom bond lengths are in Å.

For the adsorption of Li$_2$S$_n$ (n = 1, 2, 4, 6, and 8) on pristine 1T-MoS$_2$ and the defected structures, the vertical distances between two Li atoms to the surfaces were set initially according to the reported data [51] and then further adjusted by the DFT simulations of energy minimisation, see Figure 2. For the investigation of Li$_2$S$_8$ adsorption, the Li–Li bond was considered perpendicular to the 1T-MoS$_2$ (001) structures, such that the Li$_2$S$_8$ molecule lied flat above the surface, consistent with the reported optimisation results [25,51].

1T-MoS$_2$

E_{ads} = -3.30 eV

d_{Li-Sub}= 1.73, 1.86 Å

E_{ads} = -2.42 eV

d_{Li-Sub}= 2.00, 2.16 Å

E_{ads} = -2.23 eV

d_{Li-Sub}= 2.63, 2.78 Å

E_{ads} = -0.96 eV

d_{Li-Sub} = 2.92, 3.03 Å

E_{ads} = -0.77 eV

d_{Li-Sub} = 3.15, 3.26

1T-MoS$_2$-1S

E_{ads} =-4.88 eV

d_{Li-Sub}= 1.11, 1.39 Å

E_{ads} = -3.66 eV

d_{Li-Sub}= 1.54, 1.72 Å

E_{ads} = -2.70 eV

d_{Li-Sub}= 2.23, 2.49 Å

E_{ads} =-2.53 eV

d_{Li-Sub}= 0.87, 1.67 Å

E_{ads} = -1.93 eV

d_{Li-Sub}= 2.66, 2.77 Å

1T-MoS$_2$-2S

E_{ads} =-5.38 eV

d_{Li-Sub}= 1.56.1.63 Å

E_{ads} =- 5.14 eV

d_{Li-Sub}= 1.79, 1.88 Å

E_{ads} =-4.01 eV

d_{Li-Sub}= 2.53, 2.61 Å

E_{ads} = -3.10 eV

d_{Li-Sub}= 2.66, 2.70 Å

E_{ads} =-3.62 eV
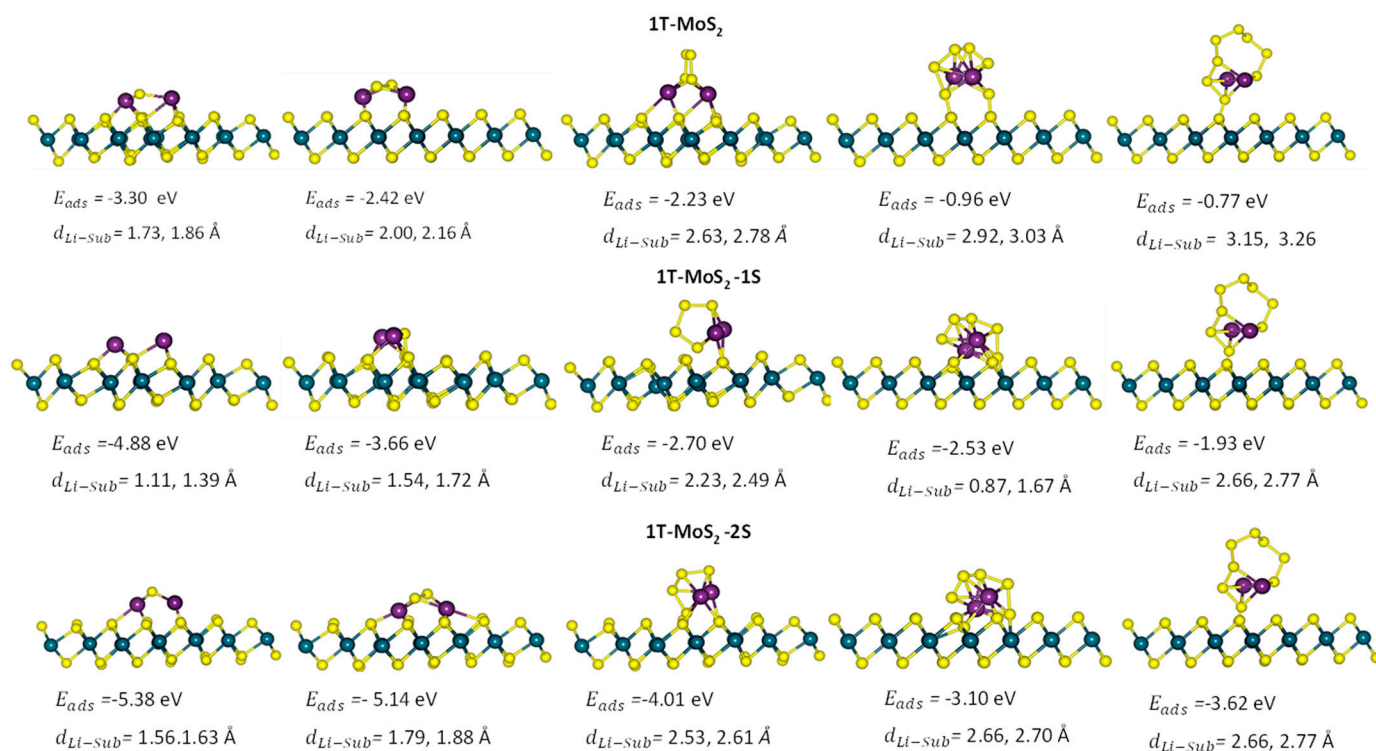
d_{Li-Sub}= 2.66, 2.77 Å

Figure 2. Side view of the optimised configurations for the examined LiPSs on the pristine 1T-MoS$_2$ and the defected structures. From top to bottom are pristine 1T-MoS$_2$, 1T-MoS$_2$-1S, and 1T-MoS$_2$-2S and from right to left are Li$_2$S$_8$, Li$_2$S$_6$, Li$_2$S$_4$, Li$_2$S$_2$, and Li$_2$S. E_{ads} and d_{Li-sub} are the adsorption energy of the system and the minimum Li-substrate distance, respectively.

Figure 3 presents the adsorption energies of the LiPSs intermediates (Li$_2$S$_n$, n = 1, 2, 4, 6, and 8) on the 1T-MoS$_2$ substrates in comparison with SACs TM-N$_4$-C (TM = Co, Fe, V, and W) and graphene. For Li$_2$S, Li$_2$S$_2$ and, especially, Li$_2$S$_4$, whose migration to the anode is critical in suppressing the subsequent cascade reactions, the strength of binding energy follows the order of graphene < Co-N$_4$-C < Fe-N$_4$-C < 1T-MoS$_2$ pristine < 1T-MoS$_2$-1S < V-N$_4$-C < W-N$_4$-C < 1T-MoS$_2$-2S. The strongest binding affinity amongst all substrates is observed for 1T-MoS$_2$-2S, with the binding energies of 5.38, 5.14, and 4.04 eV for Li$_2$S, Li$_2$S$_2$, and Li$_2$S$_4$, respectively. For Li$_2$S$_6$ and Li$_2$S$_8$, although the 1T-MoS$_2$ substrates with sulphur vacancies perform better than Co-N$_4$-C and Fe-N$_4$-C, they do exhibit weaker affinity than V-N$_4$-C and W-N$_4$-C. The observed stronger adsorption energies of the MoS$_2$ substrates with the shorter lithium polysulphide chains indicates gradually reinforced chemical interaction from the lithium ions. This is in contrast with the weakest binding strength of the single atom catalysts with Li$_2$S$_4$, especially for V-N$_4$-C and W-N$_4$-C, indicating the chance of Li$_2$S$_4$ migration to the anode before it has the chance to transform to the precipitating solid Li$_2$S$_2$ and Li$_2$S. Our results on the binding energies for the pristine 1T-MoS$_2$ showed an energy range of 0.7–3.3 eV which is in a good agreement with those of Dong et al. [26], but not completely in line with those of He et al. [47]. To the best of our knowledge, we are the first to report the binding energies of LiPSs with the defected 1T-MoS$_2$, with one and two sulphur vacancies.
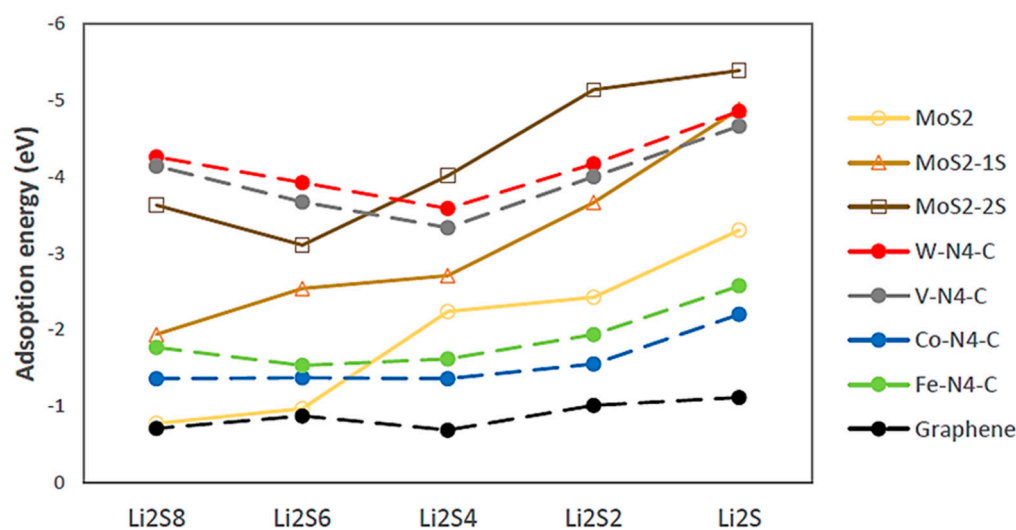
Figure 3. Adsorption energies for Li_2S_n (n = 1, 2, 4, 6, and 8) on 1T-MoS$_2$ substrates in comparison with SACs TM-N$_4$-C (TM = Co, Fe, V, and W) and graphene [17].

The higher adsorption energy for 1T-MoS$_2$ with sulphur vacancies toward LiPSs intermediates, especially the lower order sulphides Li_2S, Li_2S_2, and Li_2S_4, compared with 1T-MoS$_2$ pristine can be explained based on the charge density. Research showed that the sulphur deficiency in the MoS$_2$ structure resulted in larger charge densities of surrounding S atoms and therefore a tighter bond with Li atoms [51]. This would enhance the interaction with the LiPSs intermediates, providing more thermodynamics and kinetic driving force for binding and finally causing an increased stabilisation effect. Overall, Figure 3 illustrates that 1T-MoS$_2$-2S (two sulphur vacancies) has better capability in trapping all sulphides than 1T-MoS$_2$ and 1T-MoS$_2$-1S.

To evaluate the catalytic effect of 1T-MoS$_2$ substrates, different disproportionation reaction pathways for the slow conversion of Li_2S_4 to Li_2S were investigated:

(i)   a two-step process: $Li_2S_4 \rightarrow Li_2S_2 + S_2$ followed by $Li_2S_2 \rightarrow Li_2S + S$;
(ii) a one-step process: $Li_2S_4 \rightarrow Li_2S + S_3$.

Figure 4 depicts the optimised geometry of the adsorbed Li_2S_2 (Figure 4A–C) and its dissociated products (Figure 4D–F) on the surface of 1T-MoS$_2$ substrates for the last reaction: $Li_2S_2 \rightarrow Li_2S + S$ of pathway (i) above, as obtained by the DFT simulations. Figures S1 and S2 also show the optimised geometry of the adsorbed Li_2S_4 and its dissociated products on the surface of 1T-MoS$_2$ substrates for the first reaction: $Li_2S_4 \rightarrow Li_2S_2 + S_2$ of pathway (i) and the reaction: $Li_2S_4 \rightarrow Li_2S + S_3$ of pathway (ii), respectively. In the different structures in Figure 4, Figures S1 and S2, the separated S atom, S_2 or S_3 molecules on 1T-MoS$_2$ substrates is either on the top of the MoS$_2$ structure (1T-MoS$_2$ pristine) or embedded in the MoS$_2$ structure (1T-MoS$_2$-1S) or in the void space created by the vacancies (1T-MoS$_2$-2S).

Figure 5 shows the dissociation, E_d, and activation, E_a, energies and atomic structures of reactants and products for the disproportionation reactions of (A) $Li_2S_4 \rightarrow Li_2S_2 + S_2$, (B) $Li_2S_4 \rightarrow Li_2S + S_3$, and (C) $Li_2S_2 \rightarrow Li_2S + S$ on pristine 1T-MoS$_2$, 1T-MoS$_2$-1S, and 1T-MoS$_2$-2S. The reaction coordinate and energy change of the transition state (TS) (as found from the transition-state search method (TSS)) and product, with respect to the reactant are further presented, with the calculated E_a and E_d values. Considering the two pathways (i) and (ii), starting from Li_2S_4 to ultimately reaching Li_2S, Figure 5 illustrates that reaction pathway (ii), $Li_2S_4 \rightarrow Li_2S + S_3$, is the preferred pathway for 1T-MoS$_2$ pristine and 1T-MoS$_2$-1S cathode hosts, as the activation and dissociation energies of this reaction (which are 1.73 and 0.32 eV, respectively) are lower than those of the reactions of pathway (i) (which are 2.30 and 0.68 eV, respectively). Hence, for these two molybdenum disulphide substrates the preferred pathway could be through direct conversion of Li_2S_4 to Li_2S, by-passing

the Li_2S_2 formation step. However, for $1T\text{-}MoS_2\text{-}2S$, reaction pathway (i) is preferred, consisting of a first step of $Li_2S_4 \rightarrow Li_2S_2 + S_2$ followed by the second step of $Li_2S_2 \rightarrow Li_2S + S$, as determined from their lower relative energy change, the activation barrier and dissociation energy values which compared well with those of $Li_2S_4 \rightarrow Li_2S + S_3$. These results mean that the minimum amount of energy that must be provided to the reactant components (Li_2S_4) to lead to a chemical reaction for the $Li_2S_4 \rightarrow Li_2S + S_3$ pathway is only met on $1T\text{-}MoS_2$ pristine and $1T\text{-}MoS_2\text{-}1S$ cathodes and for $Li_2S_4 \rightarrow Li_2S_2 + S_2$ pathway is only met on $1T\text{-}MoS_2\text{-}2S$. Figure 5 further indicates a considerable activation energy difference between $1T\text{-}MoS_2\text{-}1S$ and $1T\text{-}MoS_2\text{-}2S$ throughout all reaction pathways. This can be explained based on the relationship between activation energy of a chemical reaction and its rate. In fact, molecules can only complete the reaction once they have reached the top of the activation energy barrier. Therefore, for the higher barriers, fewer molecules will have enough energy to make it over the barrier at any given moment, leading to a lower reaction rate, and for the lower barriers, more molecules will have enough energy to make it through, resulting in an increased reaction rate. Thereby, in Figure 5, very fast reaction rate for the reaction of $Li_2S_4 \rightarrow Li_2S + S_3$ on $1T\text{-}MoS_2$ pristine and $1T\text{-}MoS_2\text{-}1S$ cathodes is predicted but for the reaction of $Li_2S_4 \rightarrow Li_2S_2 + S_2$, followed by $Li_2S_2 \rightarrow Li_2S + S$, on $1T\text{-}MoS_2\text{-}2S$, a reduced reaction rate is expected.
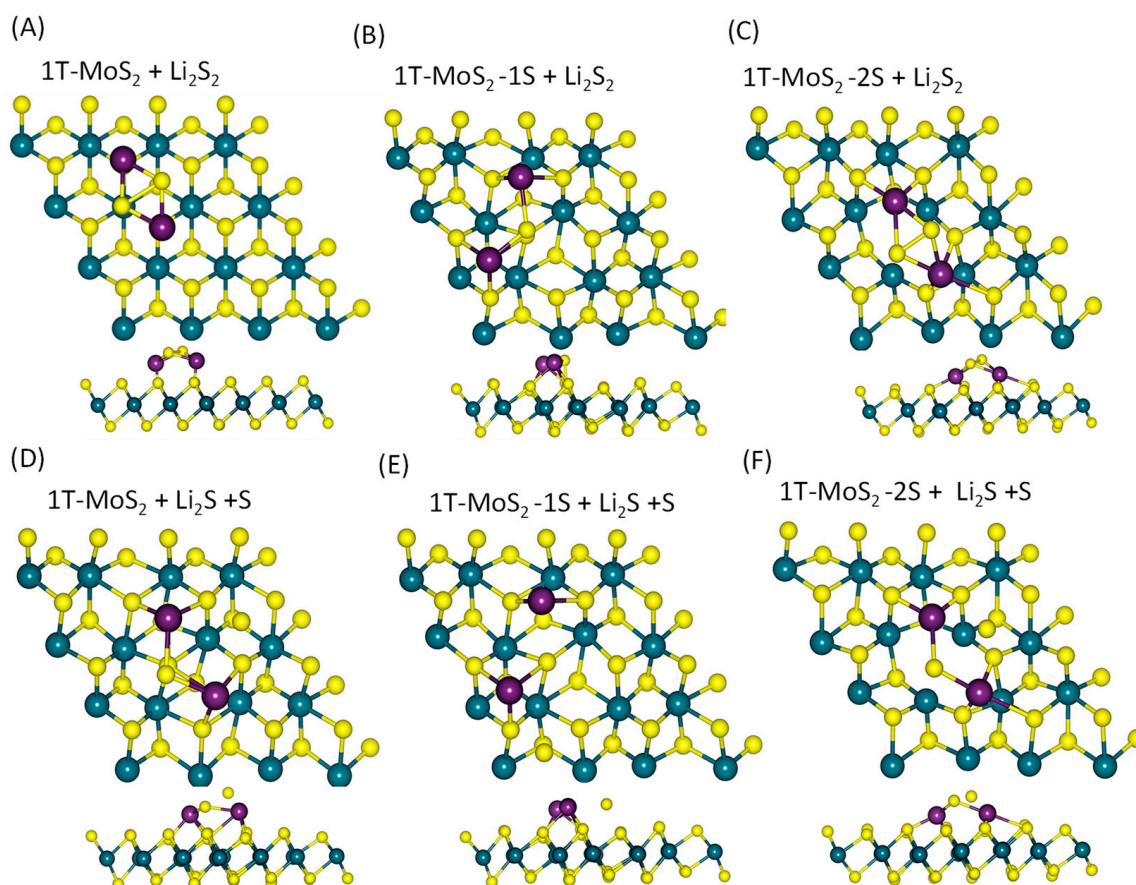
Figure 4. Top views and side views of the optimised geometry of adsorbed Li_2S_2 on (**A**) $1T\text{-}MoS_2$, (**B**) $1T\text{-}MoS_2\text{-}1S$, (**C**) $1T\text{-}MoS_2\text{-}2S$; (**D**–**F**) its dissociated products on $1T\text{-}MoS_2$, $1T\text{-}MoS_2\text{-}1S$, $1T\text{-}MoS_2\text{-}2S$, respectively. The S–S bond length was less than 5 Å.
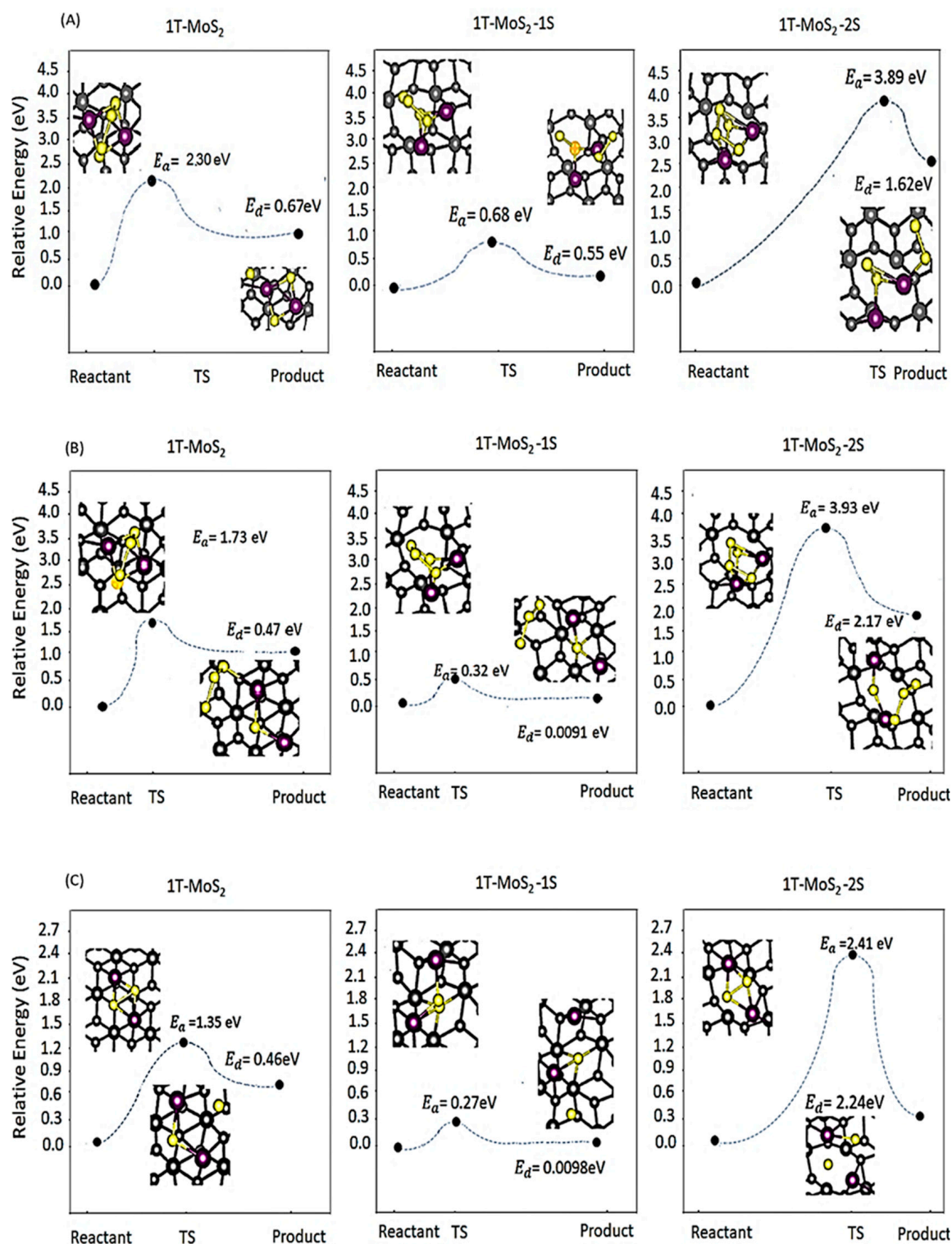
Figure 5. Dissociation energy graphs and atomic structures of reactants and products for the disproportionation reactions of (**A**) $Li_2S_4 \rightarrow Li_2S_2 + S_2$, (**B**) $Li_2S_4 \rightarrow Li_2S + S_3$, and (**C**) $Li_2S_2 \rightarrow Li_2S + S$ on 1T-MoS_2 pristine, 1T-MoS_2-1S and 1T-MoS_2-2S. The relative energy change and reaction coordinate of the transition state (TS) and product with respect to the reactant is presented in the graphs. E_a is the calculated activation barrier for the transition state and E_d is the calculated dissociation energy to break the reactants bonds.

The main observation from all the results of Figure 5 is the lowest activation and dissociation energies for 1T-MoS$_2$-1S compared to other molybdenum disulphide substrates throughout all reactions. This highlights the high catalytic activity of 1T-MoS$_2$-1S which results in spontaneous conversion reactions on the surface, with minimum energy requirement to proceed along the discharge of a Li-S battery.

A comparison of the activation energies for the typical last reaction Li$_2$S$_2$ → Li$_2$S + S on 1T-MoS$_2$ substrates against our previously published results on the single atom catalysts and graphene [17] again confirms the superior catalytic activity of 1T-MoS$_2$-1S against all studied catalysts with the lowest E_a value (E_a follows the order of graphene (2.73 eV) > Fe-N$_4$-C (1.71 eV) > Co-N$_4$-C (1.66 eV) > W-N$_4$-C (1.10 eV) > V-N$_4$-C (1.01 eV) > 1T-MoS2-1S (0.27 eV). Therefore, it is expected that 1T-MoS$_2$-1S could promote a fast LiPSs reaction and conversion to the final product.

Figure 6 displays the relative Gibbs free energy profiles for the LiPSs disproportionation reactions on 1T-MoS$_2$ substrates against graphene and TM-N$_4$-C (TM = Co, Fe, V, and W) SAC materials, where an initial spontaneous exothermic reaction from S$_8$ to Li$_2$S$_8$ is followed by a flatter profile with thermoneutral, or a small degree of exothermic or endothermic trends depending on substrate. It can be observed that the first step of Li$_2$S$_8$ production from S$_8$ reactant is the most spontaneous according to the order: 1T-MoS$_2$-2S > 1T-MoS$_2$-1S > 1T-MoS$_2$ > SACs. This means that the fastest reaction kinetics occurred on the 1T-MoS$_2$-2S surface with Gibbs free energy value of −10.14 eV for the first conversion step.
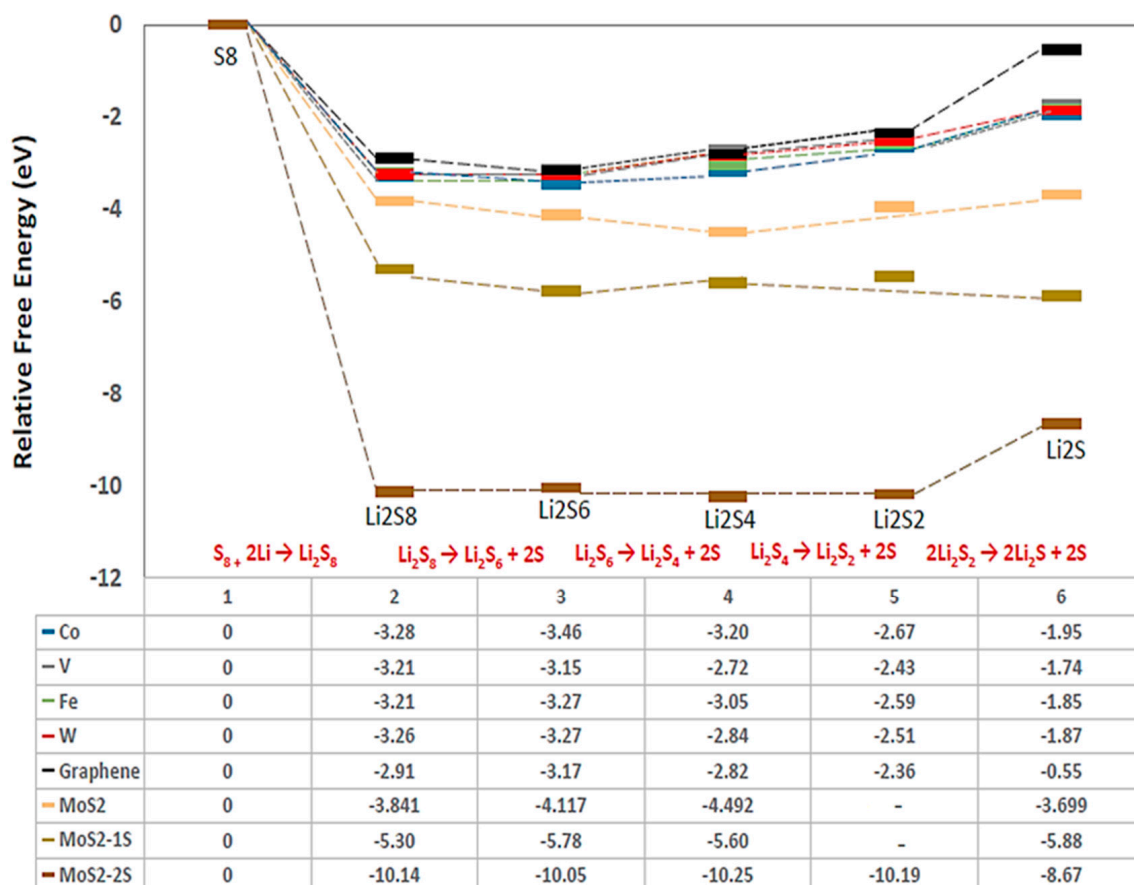

		$S_8 + 2Li \rightarrow Li_2S_8$	$Li_2S_8 \rightarrow Li_2S_6 + 2S$	$Li_2S_6 \rightarrow Li_2S_4 + 2S$	$Li_2S_4 \rightarrow Li_2S_2 + 2S$	$2Li_2S_2 \rightarrow 2Li_2S + 2S$
		1	2	3	4	5	6
— Co		0	-3.28	-3.46	-3.20	-2.67	-1.95
— V		0	-3.21	-3.15	-2.72	-2.43	-1.74
— Fe		0	-3.21	-3.27	-3.05	-2.59	-1.85
— W		0	-3.26	-3.27	-2.84	-2.51	-1.87
— Graphene		0	-2.91	-3.17	-2.82	-2.36	-0.55
— MoS2		0	-3.841	-4.117	-4.492	-	-3.699
— MoS2-1S		0	-5.30	-5.78	-5.60	-	-5.88
— MoS2-2S		0	-10.14	-10.05	-10.25	-10.19	-8.67

Figure 6. Relative Gibbs free energy for the examined disproportionation reactions on 1T-MoS$_2$ substrates in comparison with graphene and TM-N$_4$-C (TM = Co, Fe, V, and W) materials. The numerical values show the stepwise relative free-energy change of each reaction. The blank for MoS$_2$ plain and MoS$_2$-1S represents the direct conversion reaction from Li$_2$S$_4$ to Li$_2$S according to the preferred pathway for these substrates.

Referring to Figure 3 which demonstrates the adsorption energies of the different 1T-MoS_2 substrates towards Li_2S_8 are reducing, we could speculate that the amount of Li_2S_8 quantity produced on 1T-MoS_2-2S would be prevented from migrating to the anode during discharge and be ready for the next reaction step at the surface of the cathode host. The subsequent steps to Li_2S_6 and Li_2S_4 are almost thermoneutral for the 1T-MoS_2 substrates, indicating slower reactions than the first step. Thereafter, the preferred direct pathway is a little endothermic for 1T-MoS_2 and a little exothermic for 1T-MoS_2-1S, but the energy required for 1T-MoS_2 is still less than the energy required for graphene [17], demonstrating the effectiveness of 1T-MoS_2 and 1T-MoS_2-1S to reach good conversion to the final product Li_2S. The 1T-MoS_2-2S substrate guides the reaction mechanism along a two-step pathway, an almost thermoneutral step of Li_2S_4 to Li_2S_2 and a last endothermic step to Li_2S of 1.52 eV, the same as for graphene substrate [17]. The very slow reaction conversion of Li_2S_2 to Li_2S plays a major limiting role in the utilisation of sulphur in Li-S batteries and has been identified as the rate-limiting step for the conversion of LiPSs species. Amongst all three of the investigated 1T-MoS_2 cathode hosts, 1T MoS_2-1S offers the best substrate for the Li_2S_4 to Li_2S conversion, while 1T-MoS_2 without defects offers the best substrate for the Li_2S_4 production and 1T-MoS_2-2S offers the best substrate for the spontaneous Li_2S_8 production and adsorption at the surface of cathode host. Taking also into account that 1T-MoS_2-2S and then 1T-MoS_2-1S have the highest adsorption energy towards LiPSs (Figure 3), it is clear that a balance of pristine 1T-MoS_2 and defected with 1S and 2S vacancies would be best to combine the strengths of each 1T-MoS_2 material and counteract any disadvantages.

Figure 7 displays the atom-projected PDOS plots for 1T-MoS_2, 1T-MoS_2-1S, and 1T-MoS_2-2S structures, for the adsorbed Li_2S_4 and the products of the disproportionation reactions throughout the preferred reaction pathways for each substrate in the conversion of Li_2S_4 to Li_2S. The up and down spins states of electrons in the PDOS data before Li_2S_4 adsorption and throughout the conversion reactions were symmetrically distributed which reflects the non-magnetic properties of the based molecules even after the conversion reactions. It must be mentioned that here for the sake of simplicity and clarity in the graphs only the up spin states of electrons are presented in Figure 7. For the 1T-MoS_2, 1T-MoS_2-1S, and 1T-MoS_2-2S structures before adsorption of Li_2S_4, the hybridized DOS intensities for Mo and S atoms below the Fermi level, where there is a high probability of the electrons occupied-states, confirm the inherent covalent binding between the nearest neighbour atoms, in line with previous observations in the literature [53]. The DOS intensities for Mo above the Fermi level demonstrate its partly metallic character as a transition metal. This can be explained based on the availability of electrons unoccupied-states of Mo for the binding. After adsorption of Li_2S_4 on the 1T-MoS_2 substrates, the DOS intensities near-Fermi level exhibit a sudden increase for both Mo and S atoms, indicating occupation of the available states by the Li_2S_4 electrons.

Figure 8 further depicts the orbital projected PDOS plots of d, p, and s orbitals of Mo, S, and Li atoms, respectively, after adsorption of Li_2S_4 and for the dissociation reactions for all substrates. The plots reveal that the d states have coupled with the p states and have crossed the Fermi level, demonstrating a strong hybridisation between Mo d and S p orbitals throughout the disproportionation reactions. The electron doping effect of Li can also cause the chemical potentials to be shifted towards the unoccupied d bands, and therefore the composite systems to remain metallic. This confirms that the loss of energy with lithiation is plausible, as was already observed in our binding energy results (see Figure 3).
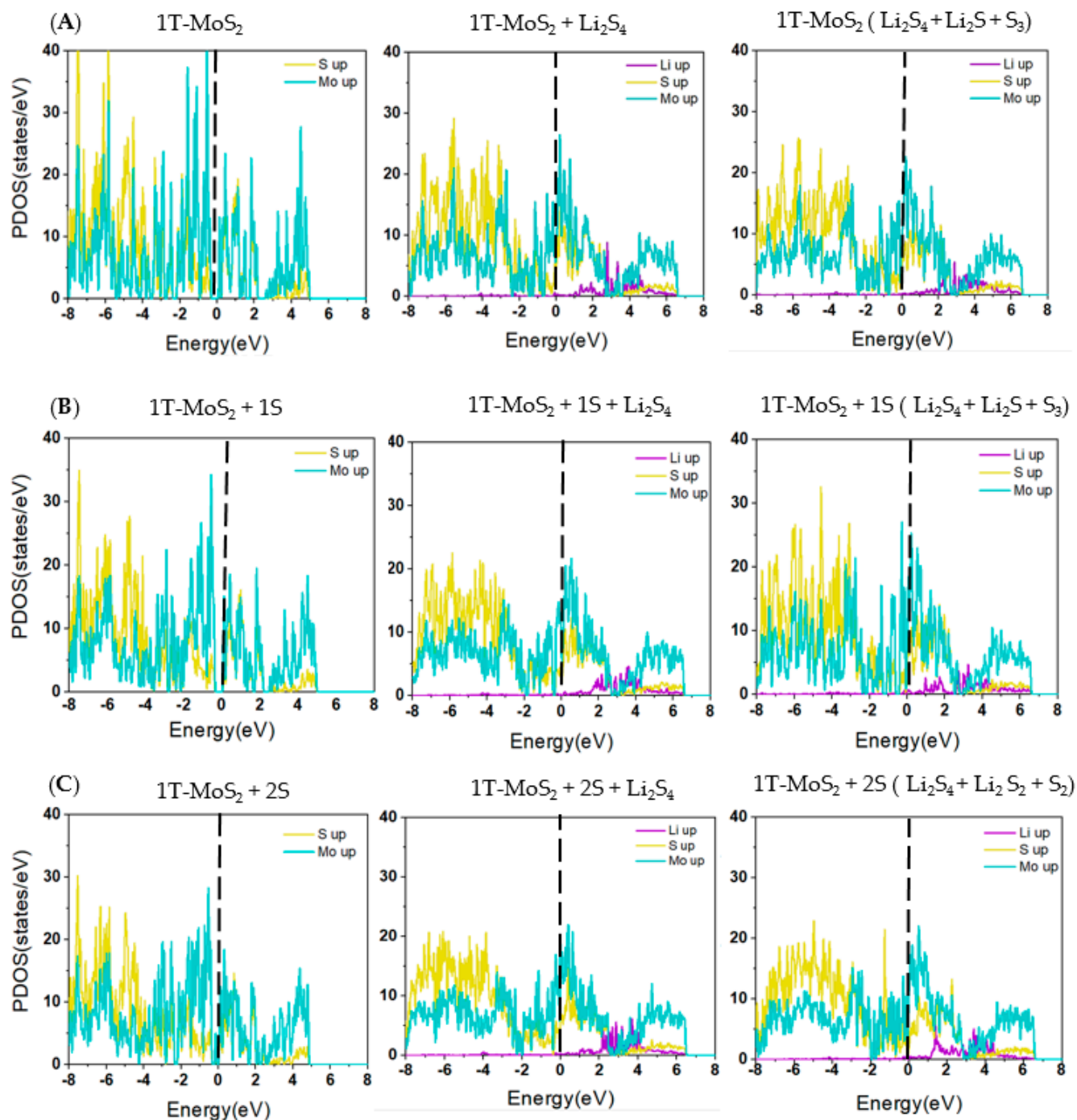
Figure 7. Spin-resolved projected DOS profiles for (**A**) 1T-MoS$_2$ pristine, (**B**) 1T-MoS$_2$-1S, and (**C**) 1T-MoS$_2$-2S for the disproportionation reactions of the preferred pathway for the conversion of Li$_2$S$_4$ to Li$_2$S. The vertical dotted lines represent the Fermi energy level.
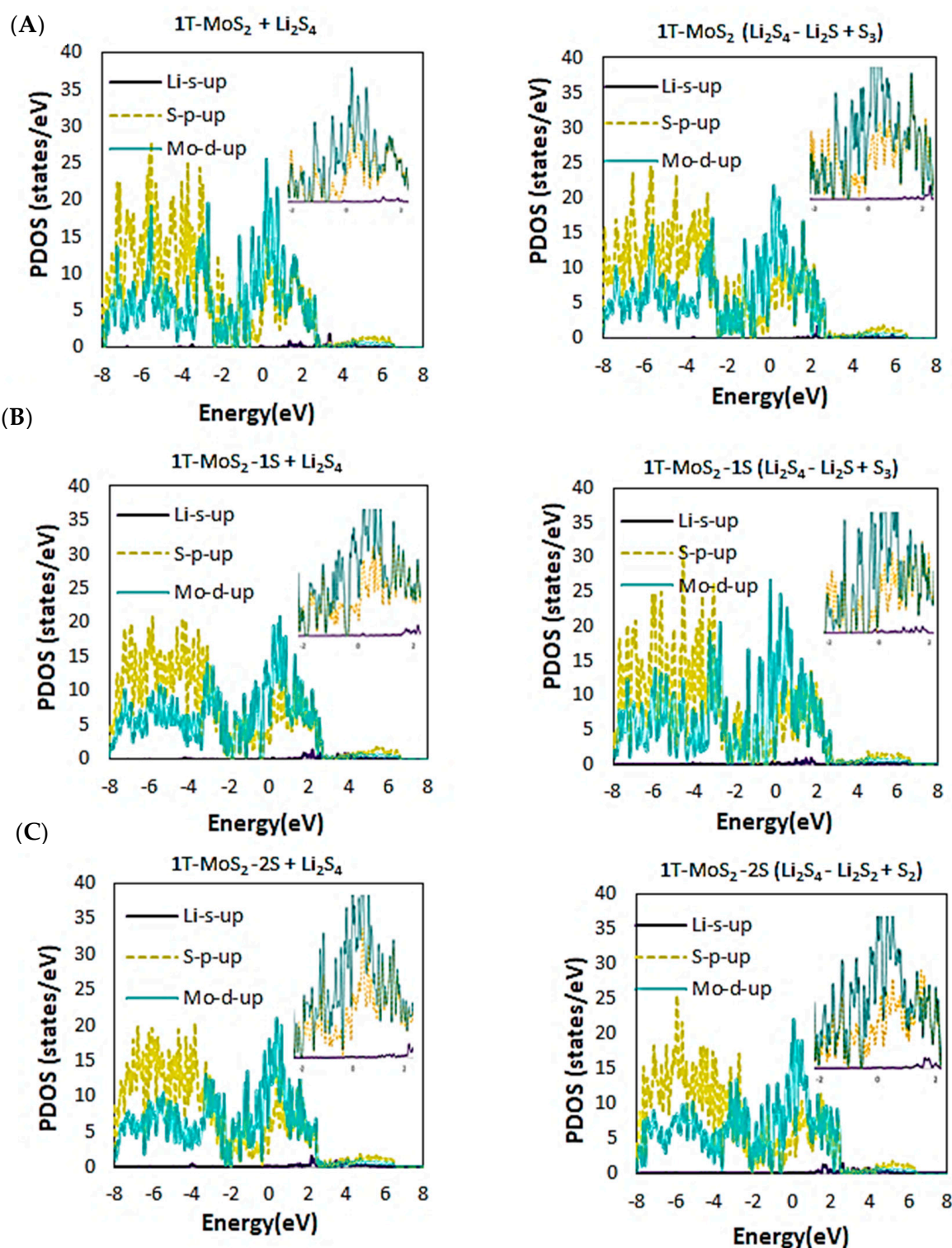
Figure 8. The orbital projected PDOS profiles for the preferred disproportionation reactions on (**A**) 1T-MoS$_2$ pristine, (**B**) 1T-MoS$_2$-1S, and (**C**) 1T-MoS$_2$-2S. The inserts show enlarged intensities around the Fermi energy levels.

　　　　Figure 9 further presents the atom-projected PDOS plots for the last reaction step Li$_2$S$_2$ to Li$_2$S of the preferred pathway on the 1T-MoS$_2$-2S substrate, where no significant horizontal shifts are observed with respect to the Fermi level but the number of probability of states has increased especially for Mo near the Fermi level and for S away from the Fermi level throughtout the conversion reaction.
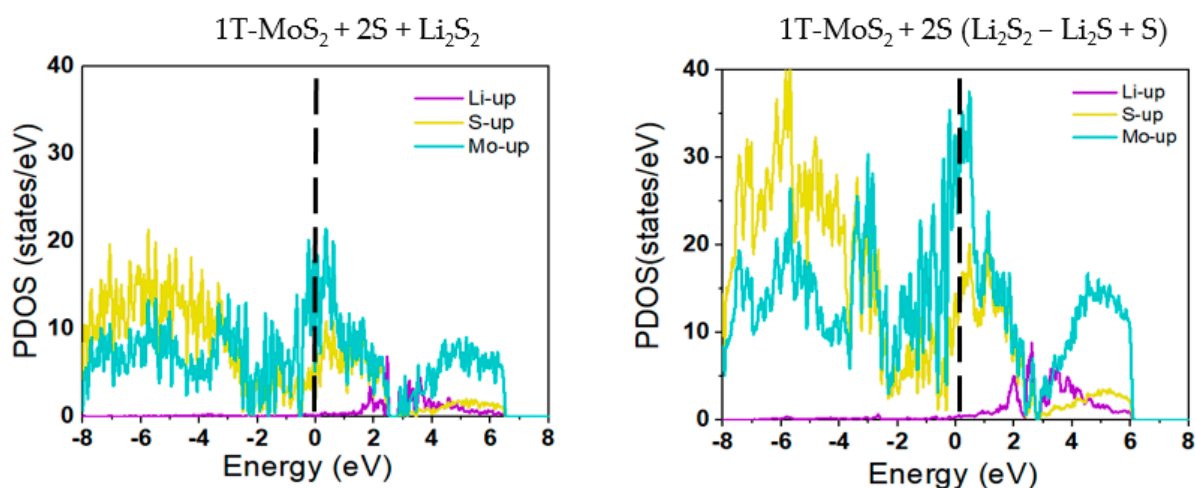
Figure 9. Spin-resolved projected DOS profiles for 1T-MoS$_2$-2S for the last disproportionation reaction Li$_2$S$_2$ to Li$_2$S conversion in the two-step preferred pathway for this substrate. The vertical dotted lines represent the Fermi energy level.

2.2. Experimental Evaluation

Based on the recommendations of the DFT simulations in Section 2.1, the 1T-MoS$_2$ material used as cathode host combines 1T-MoS$_2$, 1T-MoS$_2$-1S, and 1T-MoS$_2$-2S regions, amounting to a vacancy concentration of 6×10^{13} cm^{-2} of which 87% is 1S vacancies and 13% is 2S vacancies according to the data from material characterisation via high angle annular dark-field (HAADF) scanning transmission electron microscope (STEM) imaging from a previous study by our group for hydrogen evolution reaction [54]. Figure 10 presents the experimental data from the electrochemical testing. Figure 10A depicts a maximum specific capacity of 1190 mAh g$_S^{-1}$ and 655 mAh g$_S^{-1}$ upon discharge at 0.1C and 1C, respectively, which is superior than Li-S cells in the literature with carbon cathode hosts and the same separator and electrolyte tested in galvanostatic charge-discharge (GCD): for example, a Li-S cell with carbon nanofibre host exhibited 930 mAh g$_S^{-1}$ and 556 mAh g$_S^{-1}$ upon discharge at 0.1C and 1C, respectively [55]. The reaction plateau at 2.1 V is corresponding to the conversion of Li$_2$S$_4$ into Li$_2$S, described as the following equation (considering S$_8$ as the starting reactant in discharge): $2Li_2S_4 + 12Li^+ + 12e^- \leftrightarrow 8Li_2S$, consistent with the DFT simulations that predict this to be the preferred pathway for cathode host pristine 1T-MoS$_2$ and 1T-MoS$_2$-1S.

CV at different rates in Figure 10B displays a distinct peak upon charge and two distinct peaks upon discharge at the typical voltage positions as expected in Li-S cells [55,56]. The CV rate dependence of the overpotential and intensity of CV peaks is as expected in battery cells [57]. The polarisation at 0.2 mV s^{-1} is lower than expected, compared to the CV curve at 0.1 mV s^{-1}, because the faster scan rate of 0.2 mV s^{-1} leaves shorter time for reaction and thus the reaction is less sufficient or it might result to a large amount of sulphide production over the solution saturation point that leads to early precipitation that might block good electron transport for further reaction. The cell demonstrates good cyclability in Figure 10A,C (97% capacity retention after 50 cycles in the schedule of Figure 10C) and almost 100% coulombic efficiency in Figure 10D, all attributed to the elimination of the shuttling of polysulphides given the high adsorption energy and good electrocatalytic properties for the related cathode host material as predicted by the DFT simulations. The fall of capacity of the cell cycled at 1C in Figure 10D, from 625 to 460 mAh g$_S^{-1}$ after 200 cycles, is attributed to issues of solid precipitation (sulphur precipitation in charge or Li$_2$S precipitation in discharge) at the moderately high C-rate, rather than any shuttling effects, given that the capacity is stabilised at 460 mAh g$_S^{-1}$ after 200 cycles till a total 500 cycles tested so far.
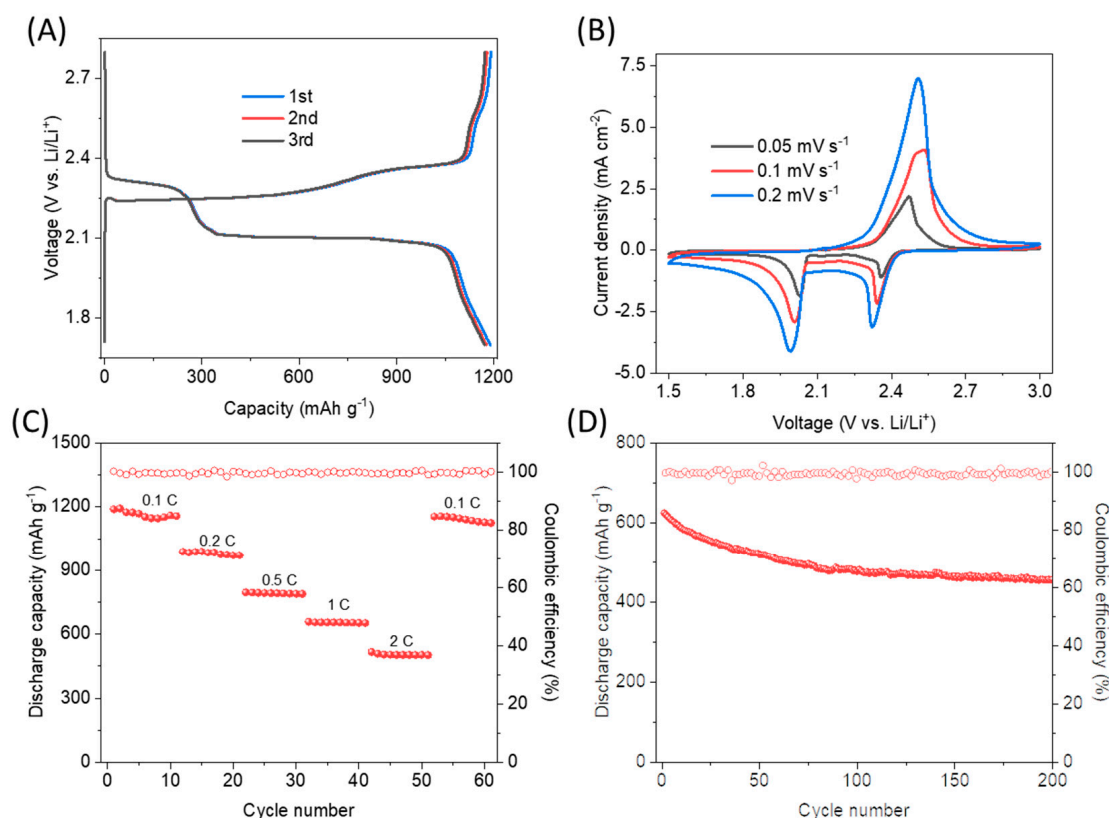
Figure 10. Experimental data from the electrochemical testing of the Li-S cell with the 1T-MoS$_2$ cathode that contains a mixture of pristine 1T-MoS$_2$, and 1T-MoS$_2$-1S, and 1T-MoS$_2$-2S: (**A**) The first three GCD (galvanostatic charge-discharge) cycles at 0.1C rate; (**B**) CV tests at different scan rates; (**C**) results of specific capacity (with respect to the sulphur mass) in discharge and Coulombic efficiency during GCD cycling at different C-rates; (**D**) results of specific capacity in discharge and Coulombic efficiency during GCD cycling at 1C.

The 1T-MoS$_2$ cathode host material of this study, combined with 1 and 2 sulphur vacancies, is a significant advance compared with relevant sulphide-based cathode hosts in the literature. For example, N-doped MoS$_2$ based on 1T/2H mixed phase MoS$_2$ [58] exhibited similarly good cyclability as displayed in Figure 10C in this study but lower discharge capacity (1030 mAh g$_S^{-1}$) at 0.1 C than our results in Figure 10A. A mesoporous carbon/ZnS/CuS nanocomposite cathode [59] reached a high specific capacity of 1457 mAh g$_S^{-1}$ at first discharge at 0.1 C but not so good cyclability after a schedule of 50 cycles at different C-rates (1000 mAh g$_S^{-1}$ at 0.1 C in cycle 45) compared to our results in Figure 10C.

3. Methods and Materials

3.1. Computational Method

The simulation framework which takes into account the atomic and electronic properties of 1T-MoS$_2$ (including pristine, defected with sulphur vacancies of 1T-MoS$_2$-1S and 1T-MoS$_2$-2S) was first implemented in VESTA software. The lattice parameters were optimised by allowing the supercell lattice vectors and ionic positions to change in a simulation box with the vacuum space of 35 Å in the Z-direction. A (4 × 4) supercell of MoS$_2$ monolayer consisting of 48 atoms, which contains 16 Mo and 32 S, was made up of the primitive cell of MoS$_2$. The supercell size was selected so that the 1S or 2S vacancy concentration in 1T-MoS$_2$-1S and 1T-MoS$_2$-2S, respectively, matched the total vacancy concentration of the material used in the experimental section of this study, reported as 6 × 10^{13} cm^{-2} in Section 2.2. CASTEP was then employed to perform all spin-polarised DFT simulations for the interaction between the lithium sulphide species and each MoS$_2$ substrate [60]. A spin

polarisation of 2 was used. The exchange and correlation potential was calculated using the generalised gradient approximation (GGA) exchange correlation function as described by Perdew−Burke− Ernzerhof (PBE) [61], and the Brillouin zone was sampled with the Monkhorst-Pack grid using a $2 \times 2 \times 1$ K-point mesh. The valence electrons identified on a plane-wave basis were used with a cut-off energy of 500 eV to ensure the precision of calculations and the tight convergence criteria (energy and force tolerance of 10^{-5} eV and 10^{-4} eV/A°, respectively). The van der Waals (vdW) dispersion correction as described by Grimme's empirical method was further considered for all the simulations [62].

3.2. Computational Models

The studied 1T-MoS$_2$ consisted of one molybdenum sheet sandwiched by two sulphur sheets, forming an S-Mo-S structure, where the weakly interacting layers were held together by van der Waals interactions. The (001) facet as the largest exposed surface [51], was selected for simulation of the catalysts. The adsorption sites were chosen at hexagonal close packed (HCP) and face centred cubic (FCC) positions on all catalysts, as recommended [51]. For the defected 1T-MoS$_2$ (001) surface, the model was constructed by deleting one or two Top site S atoms at the centre position (S-deficiency), and therefore, the additional S-deficiency position was further investigated as the adsorption site. The atoms of the catalysts were also relaxed during the optimisation process. The polysulphides modelled were: Li$_2$S$_x$, x = 1, 2, 4, 6, and 8, which are the typical polysulphides produced in Li-S batteries with electrolyte 1M LiTFSI in DOL/DME solvent mixture 1:1 *v/v* [63,64].

Regarding the investigations of the reaction pathway and catalytic effects, a model of LiPS disproportionation reactions was considered for the formation of Li$_2$S from Li bulk and S$_8$, as described by Equations (1)–(5):

$$S_8 + 2\,Li \rightarrow Li_2S_8 \tag{1}$$

$$Li_2S_8 \rightarrow Li_2S_6 + \frac{1}{4}\,S_8 \tag{2}$$

$$Li_2S_6 \rightarrow Li_2S_4 + \frac{1}{4}\,S_8 \tag{3}$$

$$Li_2S_4 \rightarrow Li_2S_2 + \frac{1}{4}\,S_8 \tag{4}$$

$$Li_2S_2 \rightarrow Li_2S + \frac{1}{4}\,S_8 \tag{5}$$

The adsorption, E_{ads}, and dissociation, E_{diss}, energies were calculated for the fully relaxed structures as:

$$E_{ads} = -[E_{(MoS_2\ sub+LiPs)} - (E_{MoS_2\ sub} + E_{LiPs})] \tag{6}$$

$$E_{diss} = E_{(MoS_2\ sub+dissosiated\ LiPs)} - E_{(MoS_2\ sub+LiPs)} \tag{7}$$

where $E_{(MoS_2\ sub\ +LiPs)}$ is the total energy of the adsorbed polysulfide on 1T-MoS$_2$ substrate, $E_{MoS_2\ sub}$ is the individual energy of 1T-MoS$_2$ substrate, E_{LiPs} is the energy of an isolated LiPs molecules in a cubic lattice with a cell length of 30 Å, and $E_{(MoS_2\ sub+dissosiated\ LiPs)}$ is the total energy of the dissociated polysulfide on 1T-MoS$_2$ substrate. The dissociation energy, E_{diss}, is the required energy to break a bond and form separate molecular fragments. The relative Gibbs free energies were calculated from the total energies of the examined configurations, based on the disproportionation reactions on the cathode host, as described by the general equation as below:

$$Li_2S_n \rightarrow \frac{m}{8}\,S_8 + Li_2S_{n-m} \tag{8}$$

The activation energy was additionally calculated from the results of the transition state search (TSS) task of DFT simulation based on the transition states between the Li$_2$S$_n$

(i.e., reactant) and decomposed Li_2S_n (i.e., product). The complete linear synchronous transit and quadratic synchronous transit (LST/QST) methods were used for the TSS task, where the root mean square forces per atom convergence criterion was set to be 10^{-3} eV/Å. The LST method performed a single interpolation to a maximum energy and the QST method alternated searches for an energy maximum with constrained minimisations in order to refine the transition state to a high degree, where their combination interpolated a reaction pathway to find a transition state.

3.3. Materials and Experimental Methods

Chemically exfoliated $1T$-MoS_2 as described in [65] was used as a cathode host in Li-S battery cells that were assembled in an argon-filled glove box. Specifically, the cathode of $1T$ MoS_2-sulphur composite (60 wt% sulphur) was prepared by vacuum filtrating the dispersion of 20 mg $1T$-MoS_2 and 30 mg sulphur powders in carbon disulphide solution (5.0 M in THF) over an anodic aluminium oxide membrane (0.02 μm pore size), followed by drying at room temperature. The areal sulphur loading was 2 mg cm^{-2}. The prepared $1T$ MoS_2-sullfur composite (60 wt% sulphur) cathode, carbon-coated aluminium foil current collector, Li foil anode, and Celgard 2400 separator were assembled into CR2032 coin cells. The electrolyte was composed of 1.0 M LiTFSI with 0.2 M $LiNO_3$ dissolved in DOL/DME (v/v = 1:1) solvents. The electrolyte/sulphur (E/S) ratio was controlled as 15 μL/mg S. The assembled Li–S coin cells were galvanostatically cycled within the potential window of 1.7–2.8 V on Land battery cycler at various C rates (1C = 1672 mAh/mgS). CV testing was also performed within the potential window of 1.5–3.0 V on biologic VSP-300 potentiostat.

4. Conclusions

In this study, first principle DFT simulations were carried out to design $1T$-MoS_2 cathode hosts for Li-S batteries, where the effect of S vacancies was evaluated by investigating pristine $1T$-MoS_2, $1T$-MoS_2-1S, and $1T$-MoS_2-2S. The investigations focussed on the adsorption properties of the $1T$-MoS_2 host materials with respect to the polysulphides Li_2S_x; x = 1, 2, 4, 6, and 8; the change of the Gibbs free energy along the reaction steps in the reaction chain to convert S_8 to Li_2S, and the electrocatalytic properties of the MoS_2 host materials and identification of the preferred pathway for the second reaction stage to convert Li_2S_4 to Li_2S that is typically slow in Li-S batteries. The results were also compared to SACs TM-N_4-C (TM = Co, Fe, V, and W) and graphene cathode hosts [17]. It was observed that the binding affinities of $1T$-MoS_2 substrates toward polysulphides with the shorter lithium polysulphide chains experienced a gradual strength, where $1T$-MoS_2-2S exhibited significant adsorption ability for all LiPSs intermediates among the examined cathode hosts.

The Gibbs free energy profiles indicated that all $1T$-MoS_2 substrates yielded more spontaneous production of Li_2S_8 than the SACs and graphene, with $1T$-MoS_2-2S and $1T$-MoS_2-1S exhibiting twice and four times, respectively, lower energy than that of SACs. Given the relatively high adsorption energy of S-vacancy containing $1T$-MoS_2 materials (3.7 and 2 eV, respectively), we believe these hosts will be able to retain the Li_2S_8 molecules in the cathode to proceed with the next reaction steps. The Gibbs energy profiles for the next two reaction steps to Li_2S_6 and Li_2S_4 showed almost thermoneutral processes for the $1T$-MoS_2 substrates with vacancies and a little exothermic reaction for the pristine $1T$-MoS_2, facilitating conversion to Li_2S_4 which is well adsorbed by all substrates. Thereafter, direct conversion from Li_2S_4 to Li_2S (solid precipitate) is the preferred pathway for $1T$-MoS_2 and $1T$-MoS_2-1S, with the reaction being a little exothermic on $1T$-MoS_2-1S, and low activation energies of 0.47 eV and 0.32 eV on $1T$-MoS_2 and $1T$-MoS_2-1S, respectively. The preferred conversion pathway on $1T$-MoS_2-2S includes two steps: a thermoneutral reaction from Li_2S_4 to Li_2S_2 with an activation energy of 3.89 eV and an endothermic reaction from Li_2S_2 to Li_2S (solid precipitate) with an activation energy of 2.41 eV. The intermediate product Li_2S_2 is highly retained on $1T$-MoS_2-2S with an adsorption energy of 5.1 eV. The conclusion was that a combination of 1S and 2S vacancies and pristine $1T$-MoS_2 would best benefit

from the specific strengths of each type of 1T-MoS$_2$. The following experimental evaluation of a Li-S battery cell with the 1T-MoS$_2$ cathode through electrochemical testing depicted very good discharge specific capacity of 1190 mAh g$_S^{-1}$ at 0.1 C-rate, 100% coulombic efficiency, and 97% capacity retention after 60 cycles in a schedule of different C-rates from 0.1 C to 2 C and back to 0.1 C. This successfully confirmed the results and design of the DFT investigation in proving that migration of the soluble polysulphides to the anode and the "shuttling" effect have been eliminated.

Supplementary Materials: The following supporting information can be downloaded at: https://www.mdpi.com/article/10.3390/ijms232415608/s1.

Institutional Review Board Statement: Not applicable.

Informed Consent Statement: Not applicable.

Data Availability Statement: Data will be provided after reasonable requests.

Conflicts of Interest: The authors declare no conflict of interest.

References

1. Zhu, K.; Wang, C.; Chi, Z.; Ke, F.; Yang, Y.; Wang, A.; Wang, W.; Miao, L. How far away are lithium-sulfur batteries from commercialization? *Front. Energy Res.* **2019**, *7*, 123. [CrossRef]
2. Bruce, P.G.; Freunberger, S.A.; Hardwick, L.J.; Tarascon, J.-M. Li–O$_2$ and Li–S batteries with high energy storage. *Nat. Mater.* **2012**, *11*, 19–29. [CrossRef] [PubMed]
3. Ding, B.; Wang, J.; Fan, Z.; Chen, S.; Lin, Q.; Lu, X.; Dou, H.; Nanjundan, A.K.; Yushin, G.; Zhang, X. Solid-state lithium–sulfur batteries: Advances, challenges and perspectives. *Mater. Today* **2020**, *40*, 114–131. [CrossRef]
4. Reece, R.; Lekakou, C.; Smith, P.A. A structural supercapacitor based on activated carbon fabric and a solid electrolyte. *Mater. Sci. Technol.* **2019**, *35*, 368–375. [CrossRef]
5. Choo, Y.; Halat, D.M.; Villaluenga, I.; Timachova, K.; Balsara, N.P. Diffusion and migration in polymer electrolytes. *Prog. Polym. Sci.* **2020**, *103*, 101220. [CrossRef]
6. Reece, R.; Lekakou, C.; Smith, P.A. A high-performance structural supercapacitor. *ACS Appl. Mater. Interfaces* **2020**, *12*, 25683–25692. [CrossRef]
7. Pei, F.; Lin, L.; Ou, D.; Zheng, Z.; Mo, S.; Fang, X.; Zheng, N. Self-supporting sulfur cathodes enabled by two-dimensional carbon yolk-shell nanosheets for high-energy-density lithium-sulfur batteries. *Nat. Commun.* **2017**, *8*, 482. [CrossRef]
8. Wu, P.; Chen, L.-H.; Xiao, S.-S.; Yu, S.; Wang, Z.; Li, Y.; Su, B.-L. Insight into the positive effect of porous hierarchy in S/C cathodes on the electrochemical performance of Li–S batteries. *Nanoscale* **2018**, *10*, 11861–11868. [CrossRef]
9. Dent, M.; Jakubczyk, E.; Zhang, T.; Lekakou, C. Kinetics of sulphur dissolution in lithium–sulphur batteries. *J. Phys. Energy* **2022**, *4*, 24001. [CrossRef]
10. Grabe, S.; Baboo, J.P.; Tennison, S.; Zhang, T.; Lekakou, C.; Andritsos, E.I.; Cai, Q.; Downes, S.; Hinder, S.; Watts, J.F. Sulfur infiltration and allotrope formation in porous cathode hosts for lithium-sulfur batteries. *AIChE J.* **2022**, *68*, e17638. [CrossRef]
11. Lasetta, K.; Baboo, J.P.; Lekakou, C. Modeling and simulations of the sulfur infiltration in activated carbon fabrics during composite cathode fabrication for lithium-sulfur batteries. *J. Compos. Sci.* **2021**, *5*, 65. [CrossRef]
12. Helen, M.; Diemant, T.; Schindler, S.; Behm, R.J.; Danzer, M.; Kaiser, U.; Fichtner, M.; Anji Reddy, M. Insight into sulfur confined in ultramicroporous carbon. *ACS Omega* **2018**, *3*, 11290–11299. [CrossRef] [PubMed]
13. Chandula Wasalathilake, K.; Roknuzzaman, M.; Ostrikov, K.; Ayoko, G.A.; Yan, C. Interaction between functionalized graphene and sulfur compounds in a lithium-sulfur battery—A density functional theory investigation. *RSC Adv.* **2018**, *8*, 2271–2279. [CrossRef] [PubMed]

14. Yin, L.-C.; Liang, J.; Zhou, G.-M.; Li, F.; Saito, R.; Cheng, H.-M. Understanding the interactions between lithium polysulfides and N-doped graphene using density functional theory calculations. *Nano Energy* **2016**, *25*, 203–210. [CrossRef]

15. Hou, T.; Chen, X.; Peng, H.; Huang, J.; Li, B.; Zhang, Q.; Li, B. Design principles for heteroatom-doped nanocarbon to achieve strong anchoring of polysulfides for lithium-sulfur batteries. *Small* **2016**, *12*, 3283–3291. [CrossRef]

16. Zhang, L.; Liang, P.; Man, X.; Wang, D.; Huang, J.; Shu, H.; Liu, Z.; Wang, L. Fe, N co-doped graphene as a multi-functional anchor material for lithium-sulfur battery. *J. Phys. Chem. Solids* **2019**, *126*, 280–286. [CrossRef]

17. Andritsos, E.I.; Lekakou, C.; Cai, Q. Single-atom catalysts as promising cathode materials for lithium-sulfur batteries. *J. Phys. Chem. C* **2021**, *125*, 18108–18118. [CrossRef]

18. Zeng, Q.-W.; Hu, R.-M.; Chen, Z.-B.; Shang, J.-X. Single-atom Fe and N co-doped graphene for lithium-sulfur batteries: A density functional theory study. *Mater. Res. Express* **2019**, *6*, 95620. [CrossRef]

19. Zhou, G.; Zhao, S.; Wang, T.; Yang, S.-Z.; Johannessen, B.; Chen, H.; Liu, C.; Ye, Y.; Wu, Y.; Peng, Y. Theoretical calculation guided design of single-atom catalysts toward fast kinetic and long-life Li–S batteries. *Nano Lett.* **2019**, *20*, 1252–1261. [CrossRef]

20. Li, Y.; Wu, J.; Zhang, B.; Wang, W.; Zhang, G.; Seh, Z.W.; Zhang, N.; Sun, J.; Huang, L.; Jiang, J. Fast conversion and controlled deposition of lithium (poly) sulfides in lithium-sulfur batteries using high-loading cobalt single atoms. *Energy Storage Mater.* **2020**, *30*, 250–259. [CrossRef]

21. Sun, M.; Wang, Z.; Li, X.; Li, H.; Jia, H.; Xue, X.; Jin, M.; Li, J.; Xie, Y.; Feng, M. Rational understanding of the catalytic mechanism of molybdenum carbide in polysulfide conversion in lithium–sulfur batteries. *J. Mater. Chem. A* **2020**, *8*, 11818–11823. [CrossRef]

22. Zhang, J.; Duan, S.; You, C.; Wang, J.; Liu, H.; Guo, S.; Zhang, W.; Yang, R. In situ-grown tungsten carbide nanoparticles on nanocarbon as an electrocatalyst to promote the redox reaction kinetics of high-mass loading sulfur cathode for high volumetric performance. *J. Mater. Chem. A* **2020**, *8*, 22240–22250. [CrossRef]

23. Liang, X.; Hart, C.; Pang, Q.; Garsuch, A.; Weiss, T.; Nazar, L.F. A highly efficient polysulfide mediator for lithium-sulfur batteries. *Nat. Commun.* **2015**, *6*, 5682. [CrossRef] [PubMed]

24. Wang, H.-E.; Yin, K.; Qin, N.; Zhao, X.; Xia, F.-J.; Hu, Z.-Y.; Guo, G.; Cao, G.; Zhang, W. Oxygen-deficient titanium dioxide as a functional host for lithium-sulfur batteries. *J. Mater. Chem. A* **2019**, *7*, 10346–10353. [CrossRef]

25. Zhou, G.; Tian, H.; Jin, Y.; Tao, X.; Liu, B.; Zhang, R.; Seh, Z.W.; Zhuo, D.; Liu, Y.; Sun, J.; et al. Catalytic oxidation of Li_2S on the surface of metal sulfides for Li-S batteries. *Proc. Natl. Acad. Sci. USA* **2017**, *114*, 840–845. [CrossRef]

26. Dong, S.; Sun, X.; Wang, Z. Trapping polysulfide on two-dimensional molybdenum disulfide for Li–S batteries through phase selection with optimized binding. *Beilstein J. Nanotechnol.* **2019**, *10*, 774–780. [CrossRef]

27. Fan, C.; Zheng, Y.; Zhang, X.; Shi, Y.; Liu, S.; Wang, H.; Wu, X.; Sun, H.; Zhang, J. High-performance and low-temperature lithium–sulfur batteries: Synergism of thermodynamic and kinetic regulation. *Adv. Energy Mater.* **2018**, *8*, 1703638. [CrossRef]

28. Hao, Z.; Yuan, L.; Chen, C.; Xiang, J.; Li, Y.; Huang, Z.; Hu, P.; Huang, Y. TiN as a simple and efficient polysulfide immobilizer for lithium–sulfur batteries. *J. Mater. Chem. A* **2016**, *4*, 17711–17717. [CrossRef]

29. Li, X.; Guo, G.; Qin, N.; Deng, Z.; Lu, Z.; Shen, D.; Zhao, X.; Li, Y.; Su, B.-L.; Wang, H.-E. SnS_2/TiO_2 nanohybrids chemically bonded on nitrogen-doped graphene for lithium–sulfur batteries: Synergy of vacancy defects and heterostructures. *Nanoscale* **2018**, *10*, 15505–15512. [CrossRef]

30. Hu, L.; Dai, C.; Liu, H.; Li, Y.; Shen, B.; Chen, Y.; Bao, S.; Xu, M. Double-shelled $NiO-NiCo_2O_4$ heterostructure@ carbon hollow nanocages as an efficient sulfur host for advanced lithium-sulfur batteries. *Adv. Energy Mater.* **2018**, *8*, 1800709. [CrossRef]

31. Liu, J.; Zhang, Q.; Sun, Y.K. Recent progress of advanced binders for Li-S batteries. *J. Power Sources* **2018**, *396*, 19–32. [CrossRef]

32. Wang, H.-E.; Li, X.; Qin, N.; Zhao, X.; Cheng, H.; Cao, G.; Zhang, W. Sulfur-deficient MoS_2 grown inside hollow mesoporous carbon as a functional polysulfide mediator. *J. Mater. Chem. A* **2019**, *7*, 12068–12074. [CrossRef]

33. Manthiram, A.; Fu, Y.; Chung, S.-H.; Zu, C.; Su, Y.-S. Rechargeable lithium–sulfur batteries. *Chem. Rev.* **2014**, *114*, 11751–11787. [CrossRef] [PubMed]

34. Al Salem, H.; Babu, G.; Rao, C.V.; Arava, L.M.R. Electrocatalytic polysulfide traps for controlling redox shuttle process of Li−S batteries. *Am. Chem. Soc.* **2015**, *137*, 11542–11545. [CrossRef] [PubMed]

35. Wang, M.; Fan, L.; Tian, D.; Wu, X.; Qiu, Y.; Zhao, C.; Guan, B.; Wang, Y.; Zhang, N.; Sun, K. Rational design of hierarchical SnO_2/1T-MoS_2 nanoarray electrode for ultralong-life Li–S batteries. *ACS Energy Lett.* **2018**, *3*, 1627–1633. [CrossRef]

36. Liu, Y.; Cui, C.; Liu, Y.; Liu, W.; Wei, J. Application of MoS2 in the cathode of lithium sulfur batteries. *RSC Adv.* **2020**, *10*, 7384–7395. [CrossRef]

37. Jayabal, S.; Wu, J.; Chen, J.; Geng, D.; Meng, X. Metallic 1T-MoS_2 nanosheets and their composite materials: Preparation, properties and emerging applications. *Mater. Today Energy* **2018**, *10*, 264–279. [CrossRef]

38. Sun, D.; Huang, D.; Wang, H.; Xu, G.-L.; Zhang, X.; Zhang, R.; Tang, Y.; Abd EI-Hady, D.; Alshitari, W.; Saad AL-Bogami, A.; et al. 1T MoS_2 nanosheets with extraordinary sodium storage properties via thermal-driven ion intercalation assisted exfoliation of bulky MoS_2. *Nano Energy* **2019**, *61*, 361–369. [CrossRef]

39. Gupta, D.; Chauhan, V.; Kumar, R. A comprehensive review on synthesis and applications of molybdenum disulfide (MoS_2) material: Past and recent developments. *Inorg. Chem. Commun.* **2020**, *121*, 108200. [CrossRef]

40. You, Y.; Ye, Y.; Wei, M.; Sun, W.; Tang, Q.; Zhang, J.; Chen, X.; Li, H.; Xu, J. Three-dimensional MoS_2/rGO foams as efficient sulfur hosts for high-performance lithium-sulfur batteries. *Chem. Eng. J.* **2019**, *355*, 671–678. [CrossRef]

41. Yu, B.; Chen, Y.; Wang, Z.; Chen, D.; Wang, X.; Zhang, W.; He, J.; He, W. 1T-MoS_2 nanotubes wrapped with N-doped graphene as highly-efficient absorbent and electrocatalyst for Li–S batteries. *J. Power Sources* **2020**, *447*, 227364. [CrossRef]

42. Dirlam, P.T.; Park, J.; Simmonds, A.G.; Domanik, K.; Arrington, C.B.; Schaefer, J.L.; Oleshko, V.P.; Kleine, T.S.; Char, K.; Glass, R.S.; et al. lemental Sulfur and molybdenum disulfide composites for Li–S batteries with long cycle life and high-rate capability. *ACS Appl. Mater. Interfaces* **2016**, *8*, 13437–13448. [CrossRef] [PubMed]

43. Hu, L.; Dai, C.; Lim, J.-M.; Chen, Y.; Lian, X.; Wang, M.; Li, Y.; Xiao, P.; Henkelman, G.; Xu, M. A highly efficient double-hierarchical sulfur host for advanced lithium-sulfur batteries. *Chem. Sci.* **2018**, *9*, 666–675. [CrossRef]

44. Abraham, A.M.; Kammampata, S.P.; Ponnurangam, S.; Thangadurai, V. Efficient Synthesis and characterization of robust MoS$_2$ and S cathode for advanced Li–S battery: Combined experimental and theoretical studies. *ACS Appl. Mater. Interfaces* **2019**, *11*, 35729–35737. [CrossRef]

45. Xu, Z.-L.; Onofrio, N.; Wang, J. Boosting the anchoring and catalytic capability of MoS$_2$ for high-loading lithium sulfur batteries. *J. Mater. Chem. A* **2020**, *8*, 17646–17656. [CrossRef]

46. Zhang, Y.; Mu, Z.; Yang, C.; Xu, Z.; Zhang, S.; Zhang, X.; Li, Y.; Lai, J.; Sun, Z.; Yang, Y.; et al. Rational design of MXene/1T-2H MoS$_2$-C Nanohybrids for high-performance lithium–sulfur batteries. *Adv. Funct. Mat.* **2018**, *28*, 1707578. [CrossRef]

47. He, J.; Hartmann, G.; Lee, M.; Hwang, G.S.; Chen, Y.; Manthiram, A. Freestanding 1T MoS$_2$/graphene heterostructures as a highly efficient electrocatalyst for lithium polysulfides in Li–S batteries. *Energy Environ. Sci.* **2019**, *12*, 344–350.

48. Lin, H.; Yang, L.; Jiang, X.; Li, G.; Zhang, T.; Yao, Q.; Zheng, G.W.; Lee, J.Y. Electrocatalysis of polysulfide conversion by sulfur-deficient MoS$_2$ nanoflakes for lithium–sulfur batteries. *Energy Environ. Sci.* **2017**, *10*, 1476–1486. [CrossRef]

49. Kamphaus, E.P.; Balbuena, P.B. Long-Chain polysulfide retention at the cathode of Li–S batteries. *J. Phys. Chem. C* **2016**, *120*, 4296–4305. [CrossRef]

50. Zhang, Q.; Wang, Y.; Seh, Z.W.; Fu, Z.; Zhang, R.; Cui, Y. Understanding the anchoring effect of two-dimensional layered materials for lithium–sulfur batteries. *Nano Lett.* **2015**, *15*, 3780–3786. [CrossRef]

51. Zhang, Q.; Zhang, X.; Li, M.; Liu, J.; Wu, Y. Sulfur-deficient MoS$_{2-x}$ promoted lithium polysulfides conversion in lithium-sulfur battery: A first-principles study. *Appl. Surf. Sci.* **2019**, *487*, 452–463. [CrossRef]

52. Assary, R.S.; Curtiss, L.A.; Moore, J.S. Toward a Molecular Understanding of energetics in Li–S batteries using nonaqueous electrolytes: A high-level quantum chemical study. *J. Phys. Chem. C* **2014**, *118*, 11545–11558. [CrossRef]

53. Jayabal, S.; Saranya, G.; Liu, Y.; Geng, D.; Meng, X. Unravelling the synergy effects of defect-rich 1T-MoS$_2$/carbon nanotubes for the hydrogen evolution reaction by experimental and calculational studies. *Sustain. Energy Fuels* **2019**, *3*, 2100–2110. [CrossRef]

54. Yang, J.; Wang, Y.; Lagos, M.J.; Manichev, V.; Fullon, R.; Song, X.; Voiry, D.; Chakraborty, S.; Zhang, W.; Batson, P.E. Single atomic vacancy catalysis. *ACS Nano* **2019**, *13*, 9958–9964. [CrossRef] [PubMed]

55. Liu, M.; Li, Q.; Qin, X.; Liang, G.; Han, W.; Zhou, D.; He, Y.-B.; Li, B.; Kang, F. Suppressing self-discharge and shuttle effect of lithium–sulfur batteries with V$_2$O$_5$-decoratChed carbon nanofiber interlayer. *Small* **2017**, *13*, 1602539. [CrossRef]

56. Shi, H.; Dong, Y.; Zhou, F.; Chen, J.; Wu, Z.-S. 2D hybrid interlayer of electrochemically exfoliated graphene and Co(OH)$_2$ nanosheet as a bi-functionalized polysulfide barrier for high-performance lithium–sulfur batteries. *J. Phys. Energy* **2019**, *1*, 015002. [CrossRef]

57. Baboo, J.P.; Yatoo, M.A.; Dent, M.; Hojaji Najafabadi, E.; Lekakou, C.; Slade, R.; Hinder, S.J.; Watts, J.F. Exploring different binders for a LiFePO$_4$ battery, battery testing, modeling and simulations. *Energies* **2022**, *15*, 2332. [CrossRef]

58. Cho, J.; Ryu, S.; Gong, Y.J.; Pyo, S.; Yun, H.; Kim, H.; Lee, J.; Yoo, J.; Kim, Y.S. Nitrogen-doped MoS$_2$ as a catalytic sulfur host for lithium-sulfur batteries. *Chem. Eng. J.* **2022**, *439*, 135568. [CrossRef]

59. Zhai, S.; Abraham, A.M.; Chen, B.; Fan, Z.; Hu, J.; Cai, Z.; Thangadurai, V. Abundant Canadian pine with polysulfide redox mediating ZnS/CuS nanocomposite to attain high-capacity lithium sulfur battery. *Carbon* **2022**, *195*, 253–262. [CrossRef]

60. Clark, S.J.; Segall, M.D.; Pickard, C.J.; Hasnip, P.J.; Probert, M.I.J.; Refson, K.; Payne, M.C. First principles methods using CASTEP. *Zeitschrift Krist. Cryst. Mater.* **2005**, *220*, 567–570. [CrossRef]

61. Blöchl, P.E. Projector augmented-wave method. *Phys. Rev. B* **1994**, *50*, 17953. [CrossRef] [PubMed]

62. Grimme, S. Semiempirical GGA-type density functional constructed with a long-range dispersion correction. *J. Comput. Chem.* **2006**, *27*, 1787–1799. [CrossRef] [PubMed]

63. Babar, S.; Lekakou, C. Molecular modeling of electrolyte and polysulfide ions for lithium-sulfur batteries. *Ionics* **2021**, *27*, 635–642. [CrossRef]

64. Lu, Y.-C.; He, Q.; Gasteiger, H.A. Probing the lithium−sulfur redox reactions: A rotating-ring disk electrode study. *J. Phys. Chem. C* **2014**, *118*, 5733–5741. [CrossRef]

65. Acerce, M.; Voiry, D.; Chhowalla, M. Metallic 1T phase MoS$_2$ nanosheets as supercapacitor electrode materials. *Nat. Nanotechnol.* **2015**, *10*, 313–318. [CrossRef] [PubMed]